Conformation switch of NPC1 epitomizes a luminal alternating access for nonpolar substrates

Xuelan Wu[1,*], Sepehr Dehghani-Ghahnaviyeh[2], Ali Rasouli[2], John A. Malona[3], Mitchell Antalek[3], Lyn H. Jones[3,4,5], Xiao Fan[6,7], Adele Peng[6,8], Emad Tajkhorshid[2,*], Hongwu Qian[9,*], Nieng Yan[6,7,10,*]

1 Department of Chemistry, Princeton University, Princeton, NJ 08544

2 Theoretical and Computational Biophysics Group, NIH Center for Macromolecular Modeling and Visualization, Beckman Institute for Advanced Science and Technology, Department of Biochemistry, and Center for Biophysics and Quantitative Biology, University of Illinois Urbana-Champaign, Urbana, Illinois 61801, USA

3 Jnana Therapeutics Inc., Boston, MA 02210

4 Present address: Department of Pediatric Oncology and Chemical Biology Program, Dana-Farber Cancer Institute, Boston, MA 02115

5 Present address: Department of Pediatrics, Harvard Medical School, Boston, MA 02115

6 Department of Molecular Biology, Princeton University, Princeton, NJ 08544

7 Present address: Institute of Bio-Architecture and Bio-Interaction (IBABI), Shenzhen Medical Academy of Research and Translation, Guangdong, China 518107

8 Present address: Tri-Institutional PhD Program in Chemical Biology, New York, NY 10065

9 MOE Key Laboratory for Membraneless Organelles and Cellular Dynamics, Division of Life Sciences and Medicine, University of Science and Technology of China, Hefei, China 230027

10 Present address: Institute of Chemical Biology, Shenzhen Bay Laboratory, Guangming District, Shenzhen 518132, Guangdong, China

* To whom correspondence may be addressed. Emails: nyan@tsinghua.edu.cn, xuelanw@alumni.princeton.edu, hongwuqian@ustc.edu.cn, emad@illinois.edu

Abstract

Niemann-Pick disease type C (NPC) arises from failure of the NPC1 and/or NPC2 proteins to mobilize lysosomal cholesterol, yet the mechanism by which the complex drives sterol translocation lacks a thorough understanding (1, 2). Here, we capture an NPC1-NPC2 complex conformation at lysosomal pH using a bis-sterol ligand (JM046), fortifying NPC2 engagement with NPC1 and enabling structural characterization of an alternative transport state. In this complex, the sterol moiety is absent from the NPC1 central tunnel, and the neck site adopts an expanded architecture that resembles a previously observed NPC1 conformation at neutral pH, indicating that the tunnel geometry is not influenced by the pH alone. Instead, we provide evidence that cholesterol occupancy in the neck site is a key determinant of tunnel contraction. Supporting this notion, NPC1 purified from cholesterol-auxotrophic insect cells exhibits a similar expanded neck conformation. Integrating these structures and molecular dynamics (MD) simulations exploring the directional cholesterol handoff from NPC2 to the NPC1 tunnel, we propose a substrate-induced gating cycle where luminal and membrane-facing openings of NPC1 switch states in a coordinated manner to transfer cholesterol across the hydrophilic glycocalyx. This mechanism is reminiscent of the alternating access mechanism for hydrophobic substrate transfer. This framework synthesizes NPC1 conformational states into a mechanistic basis to classify pathogenic NPC variants by relevant transport steps, which will illuminate mechanism-guided therapeutic strategies.

Significance Statement

Niemann–Pick type C is a severe neurodegenerative disorder caused by genetic defects in cooperating proteins NPC1 and NPC2, leading to lysosomal cholesterol accumulation. NPC2 delivers cholesterol to the membrane protein NPC1 for lysosomal egress. Using cryo-electron microscopy, we captured an NPC1–NPC2 complex state stabilized by a bis-sterol ligand, revealing that the NPC1's internal tunnel may exist in expanded and contracted forms depending on cholesterol occupancy. Integrating structural snapshots with molecular dynamics simulations, we propose a substrate-driven alternating gating cycle where the tunnel transitions between lumen-facing and membrane-facing states. This establishes a unique transport paradigm for highly hydrophobic cargoes. The framework supports mechanism-based stratification of NPC1 pathogenic subtypes to guide therapeutic development.

Main Text

Introduction

The lysosomal cholesterol transporter proteins, NPC1 and NPC2, exemplify collaborative intra-organelle transportation of hydrophobic substrates (3, 4). Defects of the pair could cause cholesterol and sphingolipid accumulation in the late endosome/lysosome (LE/Ly) system, leading to a wide variety of onset-dependent pathophysiological manifestations represented by hepatosplenomegaly, ataxia and neurological disorders (5–7). This autosomal recessive orphan disease, named Niemann-Pick disease type C, was not clinically well described until the early 2000s (8–11). Due to lack of awareness and accurate diagnosis, medical records across different countries reported incidence rates varying from 0.35 to 2.2 per million in the past century (12–15). A recent estimation of prevalence worldwide in 2016 has updated the overall incidence rate in both children and adults to 1/19,000 to 36,000 with an inclusion of two mildly symptomatic variants (16). Currently, there is only one FDA-approved drug, Miglustat, that can moderately ameliorate the symptoms by slowing down glycosphingolipid synthesis (17–19), while no cure has been found, especially given the phenotypic and mechanistic diversity (9, 11, 20). There is, however, growing research for diagnostic methods and more effective treatments (21–24). Among these efforts, deciphering the working mechanism of the NPC1-NPC2 pair paves the way

to a better understanding of both the biological process of cholesterol trafficking (25, 26) and the etiology of NPC-causing mutations (27–29).

When exogeneous cholesterol and sphingolipids are disassembled from low-density lipoprotein (LDL) vesicles in the LE/Ly system (30, 31), the soluble 151-amino acid sterol transporter NPC2 binds unloaded cholesterol in its sterol-affinitive pocket as a form of solubilization (32–34). Upon cholesterol loading, NPC2 undergoes a conformational change that exposes the hydrophobic loops and elevates its binding affinity to NPC1 (35, 36), a 1278-amino acid cholesterol transporter on the lysosomal membrane (37, 38). NPC1, too, has a deep sterol-binding pocket situated for a safeguarded cholesterol reception in its luminal N-terminal domain (NTD) (39, 40).

A general scheme of cholesterol delivery between the two proteins has been put together through a series of studies over the last decade: the cholesterol-bound NPC2 first binds the middle-luminal domain C of NPC1 (35, 41), with the sterol pocket facing NTD, and bends over to align with the pocket in NTD of NPC1 (42). It was hypothesized that the hydrophobic substrate is then transferred as the two pockets form an elongated and shielded tunnel (39, 43). After cholesterol transfer, the apo-NPC2 undergoes a conformational shift that lowers its affinity to NPC1 and prepares it for a new round of cholesterol recruitment (36, 44). The cholesterol bearer domain of NPC1, NTD, sits atop of the pseudo-symmetrically positioned middle luminal domains C & I, but it is not covalently linked to them (45). A long and flexible polyproline linker connects it to the first transmembrane (TM) domain, granting the NTD a broad degree of freedom in motion. The domain is known to be volatile and thus often missing from NPC1 structures (46, 47). Molecular dynamics (MD) studies have suggested that cholesterol binding stabilizes the NTD (48). Our previous electron cryo-microscopy (cryo-EM) studies have captured and resolved possible states of the NTD in full-length NPC1 while bound to cholesterol and/or NPC2 at a lysosomal pH of 5.5 (42). These structures revealed that the NTD has at least two intermediate states, one with the sterol pocket facing the NPC2 binding site and the other with the pocket opened towards an internal tunnel formed in between domains C & I. Coincidentally, in a structure of a topologically analogous protein, NPC1-Like-1 (NPC1L1), the NTD of NPC1L1 was captured at the tunnel-docking state when bound with its inhibitor (49).

There is yet no solid evidence on how the substrate passes through the internal tunnel. A sterol-like density was seen sitting at the region in between the middle luminal and TM domains, known as “the neck region”, in an EM reconstruction from our previous work when NPC1 is purified at pH 5.5 without additive cholesterol (42). However, the sterol molecule does not seem to be allowed a nearby outlet as the tunnel is closed in this specific conformation. On the other hand, in a structure of the protein purified at pH 8.0, a relatively expanded tunnel is observed (42). We speculated a lower pH as the trigger for sterol captivation and tunnel conformational shift in NPC1. The structure of Niemann-Pick type C-related protein-1 (NCR1), the yeast counterpart of NPC1, has also revealed distinct conformations of the transporter that are correlated with pH changes (50).

Reviewing all the structural evidence and remaining questions, we aim to investigate how different conformational states connect to each other and what drives the equilibrium to spontaneously pass down cholesterol to the membrane. Here, we stitch the scattered pieces of evidence together and put forward a spatial-temporal sequence of NPC proteins-mediated cholesterol delivery. We propose with this sequence a "luminal alternating access" model where the "expanded" and "contracted" states of NPC1 are connected to its transporter function based on a cryo-EM structure of the NPC1-NPC2 complex treated with a bis-sterol at pH 5.5, a cholesterol-free, low pH NPC1, and MD simulations that map the putative intermediate movements during NPC2 cholesterol hand-off and NTD re-orientation.

Results

Structural determination of a bis-sterol bound NPC1-NPC2 complex

It has been shown from the structure of the NPC1-NPC2 complex that cholesterol-loaded NPC2 exhibits a tendency to bend toward NPC1-NTD upon binding at NPC1-Domain C (42). Due to the rapid cholesterol exchange between NPC1-NTD and NPC2, the sterol pockets of the two in the best resolved EM map stay 13 Å apart rather than forming an elongated tunnel (42). The fact that NPC2 readily dissociates from NPC1 after clearing its sterol pocket also contributed to the instability and a small particle pool during data processing. To further stabilize the complex, we designed bis-sterol molecules, where two cholesterol molecules are covalently engineered to form one bi-functional sterol analog aiming to insert into the NPC2 pocket at one end and NPC1-NTD at the other (Fig. 1A). With a spacer between the two sterol cores ranging from 4 Å to 10 Å, the analogs are thought to replace the fluid occupancy of cholesterol and lock the two domains at a closest distance during the cholesterol hand-off (Fig. 1A).

One of the compounds, JM046, led to a complex map with closely positioned NPC2 and NPC1-NTD when prepared at a NPC1:NPC2:JM046 molar ratio of 1:5:5. The rest of the protocol, such as buffer conditions and sample preparation, was kept the same as that of the native NPC1-NPC2 complex (42). Particularly, the new complex was also prepared at pH 5.5. In contrast to the native complex, we name this complex the "bis-sterol bound", drawing contrast to the "native" complex. Utilizing 979 movie stacks, we eventually determined the cryo-EM map of the bis-sterol bound complex at a resolution of 3.2 Å (Fig. 1B, S1, Table S1). Compared with the 4.0-Å native complex, the JM046 dataset yielded a higher-resolution map from only 14% of the micrographs collected on the same microscope, implying improved complex stability in the presence of JM046. During our data processing, 2D projections of dimeric particles were seen during the 2D classification of bis-sterol locked NPC complex (Fig. S1C). Further, the orientations of two monomers are consistent with those in the NPC1L1 dimer (51), mitigating against the probability that this class merely resulted from overlapping particles. The number of particles and views, however, was insufficient for 3D map reconstruction.

Given that the bis-sterol compounds, JM046, is anticipated to link NPC2 and NTD to form the hydrophobic sterol transport tunnel, we applied a mask covering the extracellular domains (ECDs) of the complex to achieve improved local resolution at this region. The resulting 3.5-Å EM map exhibited enhanced resolution for NPC2 and NTD region, allowing more accurate side chain assignment in this area (Fig. S1E).

Following the protein assignment, we observed a sterol-like density in the cholesterol binding pocket of NPC2 within the 3.5-Å EM map. Additionally, a linear density connected to this density was observed at low thresholds, reminiscent of the link between the two sterol moieties in the JM046 (Fig. S2A). However, this density could not be accurately fitted with the bis-sterol molecule JM046 because the sterol-like density at the opposite end of the linear density was not detected (Fig. S2B). This absence is likely due to the sterol on the other end being highly dynamic. Consequently, this density may represent the sterol at one end of JM046 inserted into NPC2, while the other sterol remains exposed without occupying the NTD pocket as we designed

(Fig. S2C). There are two possible reasons for such deviation: (1) some endogenous molecules may occupy the sterol-binding site of the NTD, impeding the binding of the sterol moiety from JM046, as indicated by the presence of extra density in the cholesterol binding site of NTD (Fig. S2A); (2) JM046 may not conform to the strict stereochemical requirements necessary for the transient state, as the observed linear density doesn't align with the orientation needed to access the cholesterol binding pocket in the NTD (Fig. S2C). Nevertheless, the improved resolution provides more accurate structural information for the interaction between full-length NPC1 and NPC2 (Fig. 1C, S1F).

The 3.2-Å final map led to a model showing distinct difference to the native NPC1-NPC2 structure, NPC2 positioning slightly closer to NTD (Fig. 1D) and a neck site void of any sterol moiety. Below, we first focus on the movement of NPC2 to NTD firstly, and after that, we discuss the sterol moiety at the neck site of NPC1. Despite this movement of NPC2 towards to NTD, the relative positions of the NTD to domain I and NPC2 to domain C remain unchanged (Fig. 1E), indicating NPC2-domain C and NTD-domain I undergo rigid body movement during these conformational changes.

MD simulation suggests cholesterol binding informs its own sequential delivery

To investigate transient interactions and continuous motions that are not captured in cryo-EM structures, we used the molecular model built from bis-sterol locked NPC complex map and carried out extensive all-atom MD simulations of a membrane-bound model using NAMD (52, 53) . The lipid patches are composed of 70% POPC, 10% DOPG, 10% DPSM and 10% cholesterol. Simulations were all done with 3 replicates with randomized initial lipid placement, each for 500 ns. Two starting conditions are explored with cholesterol molecules selectively placed in NPC2 only (NPC2+CHO), and NTD only (NTD+CHO). In the NTD+CHO condition, apo-NPC2 is arbitrarily bound to NPC1 for the purpose of comparison.

As a measure of domain movement throughout the simulated motion, the angle between the membrane normal and the vector that connects the center of the mass (CoM) of NPC2-V57 and CoM of L78 is designated α, and that between the membrane normal and the vector connecting the CoMs of NPC1-Q79 and L176 is designated β (Fig. 2A). In this regard, the larger α is, the more inclined NPC2 is toward NTD. A larger β, then, means the NTD pocket lifts further upward for substrate reception from the NPC2 pocket. In the initial position, α = 102.8° and β = 46.7° (Figure 2B, dashed lines).

Under the NPC2+CHO condition, α adopts a narrow distribution with adjacent peaks at 105° and 120° (Fig. 2B, left red). β under this condition is predominantly at 55° (Fig. 2B, right red; Fig. 2C, left). This indicates that cholesterol bound NPC2 exhibits a preferred state with closer proximity to NTD, while apo-NTD tends to search for interactions with NPC2 (Movie S1).

In contrast, under the NTD+CHO condition, α peaks fall in the range of 80° to 100° (Fig. 2B left, blue), and β stays at very low angles around 0° to 30° (Fig. 2B right blue, 2C right). The cholesterol-bound NTD pocket almost turns vertical in the first 75 ns, opening up the upper tunnel and docking the substrate onto the middle luminal domains (Fig. 2C right, Movie S2). This conformation persists through the remaining 425 ns of the simulation. This scene is reminiscent of the vertical NTD orientation observed in the cryo-EM structure of ezetimibe-bound NPC1L1 (49). We also assessed the movement of the NTD relative to domain I by measuring the distance between the CoM of residues within 6 Å of the tail of the cholesterol (Fig. S3A) in the NTD (residues L89, P90, L176, Y192, M193, N198, Q200) and CoM of the triple Asn motif, N944, N945 and N948 (Fig. 2D). This parameter shows that the NTD moves closer to domain I upon cholesterol binding at the NTD (Fig. 2E).

We added a simulation where both sterol-binding pockets are occupied (NPC2+CHO & NTD+CHO) as an imitation of the state captured by JM046. We see both angles spanning wider ranges, β across 25° to 65° and α in a bimodal Gaussian distribution at 90° and 135° (Fig. S3B,

Movie S3). This hypothetical condition may give the substrate-loaded NTD a conundrum, where it tends to pass cholesterol down to the tunnel but is also prompted by NPC2 for cholesterol reception. Here, we see the two domains moving closest to each other, with two cholesterol molecules aligning end-to-end starting at 200 ns (Movie S3).

NPC1 exhibits sterol-dependent tunnel contraction and expansion

After a stabilized inter-molecular delivery, cholesterol is speculated to enter the elongated and polarity-repellant tunnel inside NPC1 (42) . There is no sterol density observed in the elongated tunnel in bis-sterol bound NPC1-NPC2 complex structure (Fig. 3A). Concurrently, the neck site differs from the native complex structures at pH 5.5 in that it is more relaxed as neck helix 2 and TM2 expand outward (Fig. 3, A&B), resembling the structure obtained at pH 8.0 previously (42). The positions of hydrophobic residues surrounding the neck site deviate as the local chemical environment changes (Figure 3B, inset). This suggests that the previously observed neck contraction may not be due to the change of pH level alone (42), because the new complex structure was determined at pH 5.5 as well. Our structure now gives rise to the hypothesis that the switch between expansion and contraction states of neck site is also sterol dependent. Here, we restate the close-ended, narrow tunnel conformation as “the contracted state” of NPC1 as native NPC1-NPC2 structure exhibits and the widened, comparatively distended neck site posture as “the expanded state” like the bio-sterol bound NPC1-NPC2 structure.

In a search for conformational components present in the dataset, we performed a 3D Variability Analysis (3DVA) on cryoSPARC with particles from a slightly less strict classification. Even though Homogeneous Refinement outputs an average density at the expanded state with a reported resolution of 3.1 Å (Fig. S1), the 3DVA result displays a series of motion alternating between the contracted and the expanded state (Movie S4), meaning the pool of particles contains a small portion that falls in the contracted state. The transition between 3DVA frames shows that the Neck helix 2-TM2 curls outward as NPC2 docks. The region relaxes to a relatively straight helix as the upper tunnel opens for NTD. Other than the neck site arrangement, NPC2 tilting angle also changes as the states switch: its bending toward NTD is concomitant with tunnel expansion (Fig. 3C). Intriguingly, the contrast between the starting and ending frames of the 3DVA result resembles that between the native and bis-sterol bound complex maps (Fig. 3A).

To this end, we wonder if the absence of cholesterol in NPC1 alone could lead to tunnel expansion. To assess this hypothesis, we expressed the same hNPC1 sequence in the cholesterol auxotrophic insect cell line *Spodoptera frugiperda* (Sf9) (54, 55) . Unlike mammalian expression systems, the relatively low-sterol environment of Sf9 minimizes the co-purification of strongly bound endogenous cholesterol (56, 57) , allowing us to capture NPC1 with largely unoccupied sterol-binding pockets. The map of NPC1-Sf9 at pH 5.5 was resolved at 3.1 Å (Fig. 3D, Fig. S4), showing an expanded state without any sterol density at the neck site (Fig. 3D, inset, Fig. S5A-C). This indicates that NPC1 can be at a neck expanded state at lysosomal pH, and cholesterol loading is a necessary condition for NPC1 tunnel contraction.

This concept offers a credible rationale for the structural discrepancy between neck conformations observed in our full-length NPC1 and previous NPC1 (ΔNTD) crystal structures(46, 47). Despite their preparation under the same pH level of 5.5, our full-length structure reveals a contracted tunnel containing sterol density, while the crystal structures exhibit an expanded tunnel without sterol occupancy. This could be attributed to the truncation of the NTD in the crystal structures, which precludes cholesterol access to the tunnel. The cholesterol-dependent nature of neck contraction thus underlies the observed disparity.

Sterol affinity around the TM domain suggests an exit path

The equilibrated MD models of NPC1-NPC2 complex under NPC2+CHO and NTD+CHO conditions, referred as NPC1-NPC2 (MD, NPC2+CHO) and NPC1-NPC2 (MD, NTD+CHO), respectively, are selected to show structural differences at the neck site of these two conditions

under the simulation. Supporting our previous description, the NPC1-NPC2 (MD, NPC2+CHO) and NPC1-NPC2 (MD, NTD+CHO) structures exhibit drastic changes in Neck helix 2-TM2 segments (Fig. 4A). To quantify and profile the bentness of this helical segment, we define the angle between the first principal axes of backbone atoms in R607-D618 (Neck helix 2) and those in F622-L637 (TM2) as θ and plot its distribution throughout the NPC2+CHO (red) and NTD+CHO (blue) simulations (Fig. 4B). A higher angle value represents a more bent helix and corresponds to a more expanded neck region. When cholesterol is in NPC2 pocket, the angle distribution rises up towards the 30-40° range. Whereas the angle stayed lower than 20° majority of the time under the NTD+CHO simulation (Fig. 4C). This points to a correlation between kink angle increase, which represents an extending neck region, to a cholesterol-bound NPC2 (Movie S1), concurring with the observation in 3DVA (Movie S4).

After release from the tunnel, the cholesterol was proposed to bind at SSD, whose corresponding domain has been found to bind sterol analogs in Ptch1, SREBP-cleavage activating protein (Scap), and NPC1L1 (58). The slanted helices of TM2 and TM3 at SSD form a nonpolar slide extended from the end of central tunnel. With Caver 3.0 for tunnel searching (59) , the resulting exit paths of bis-sterol bound complex, and NPC1-NPC2 (MD, NPC2+CHO) model show an increased exit radius at SSD entrance compared to the native complex (Fig. 3B, 4D). Multiple residues along this slide, P691, I685, Y628 and L695, have also been proven critical to cholesterol transport (Fig. 4D) (6, 27). However, sterol densities at NPC1 TM regions have been hard to capture. In contrast to NPC1L1, whose function is to keep cholesterol in custody during a clathrin-mediated endocytosis (60–62) , NPC1 may be functionally disadvantaged to capture this state because of the transient nature of cholesterol interaction with its SSD. To search for *in silico* evidence of potential sterol binding sites around SSD, we employed coarse-grained simulation for a scan in the 7-Å vicinity around the entire TM domain.

A total of six sites with a high probability of cholesterol clustering are found around the designated vicinity. Three of them sit along the aforementioned nonpolar slide of SSD and one along a similar groove at SSDL (Fig. 4E). The latter site has been considered to accommodate a lipid molecule in our previous structure (42) . This result is consistent with the three sterol densities found in NPC1L1-SSD under cholesterol-rich condition(63).

Discussion

The canonical alternating access model posits that membrane transporters undergo coordinated conformational transitions to alternately expose a substrate-binding site to opposite sides of a membrane. Traditionally characterized by "inward-facing" and "outward-facing" states, this model ensures the vectorial translocation of substrates against or along gradients (64–66) . Here, we establish that NPC1 employs a highly specialized, substrate-driven variation of this mechanism—a transition between “lumen-facing” and “membrane-facing” states to chaperone the highly hydrophobic cholesterol across the hydrophilic, glycocalyx-coated lysosomal lumen (67, 68).

Our structural and *in silico* results unveil the mechanistic sequence deduced from consecutive events during NPC-mediated cholesterol transport. In our interpretation, cholesterol binding at each step drives the next conformational shift, giving rise to a chain of alternating motions (Figure 4F).

The process initiates with cholesterol-loaded NPC2 binding to domain C and leaning toward the NPC1-NTD (Figure 4F, step 1), a movement that triggers the expansion of the tunnel’s neck site and likely facilitates the release of a previously trapped cargo (Figure 4F, step 2). Upon delivery of cholesterol to the NTD, the empty NPC2 dissociates. Driven by the affinity for the tunnel opening and anchored by electrostatic interactions, likely, between D944/D945/D948 (Domain I) and R96 (NTD), the loaded NTD undergoes a nearly 40º rotation to align vertically with the tunnel (Figure 4F, step 3). The subsequent insertion of cholesterol into the tunnel

induces a contracted state at the neck site (Figure 4F, step 4), preparing the machinery for a new cycle that reverts the protein to an expanded state upon cholesterol depletion (Figure 4F, step 5).

The alternation between the contracted state and the expanded state could result from the inclination of a second loaded NPC2 when the next delivery cycle begins (Fig. 4F, brown dashed arc to the left), or an NPC2-independent cholesterol depletion in the tunnel that converts the protein to an expanded state, as seen in NPC1-5.5 (Sf9) structure (Fig. 4F, brown dashed arrow to the right). Possible NPC2-independent external driving forces for cholesterol depletion include binding of downstream carriers, diffusion of cholesterol into the membrane system, or ion-facilitated co-transportation in NPC1.

What we have also consistently observed across structural comparison with and without cholesterol is that the tunnel entrance (towards the NTD docking site) is more closed as the neck site expands. For example, the domains C and I are slightly closer together around the tunnel opening in the bis-sterol bound complex, which also holds a more expanded neck site than the native complex (Fig. S5D). When we compare NPC1 alone, the cholesterol-free and neck expanded NPC1-Sf9 also displays comparatively tightened tunnel entrance than the neck contracted NPC1-5.5a (Fig. S5E). This anti-correlation between the tunnel entrance opening and the neck site expansion suggests that the NPC1 tunnel only opens one accessible end at a time, functioning as a dynamic seesaw switching between “lumen-facing” and “membrane-facing” states.

This sophisticated alternation is a defining hallmark of the resistance-nodulation-division (RND) superfamily, to which NPC1 belongs (69, 70). A quintessential member of this family, the bacterial multidrug efflux pump acriflavine resistance protein B (AcrB), provides a well-established structural precedent for handling highly hydrophobic or amphiphilic substrates. Driven by a proton gradient, AcrB utilizes a functionally rotating mechanism through substrate access, binding, and extrusion states (71–74). This coordinated peristaltic motion ensures that the entry and exit are never open simultaneously while squeezing the hydrophobic compound forward (75) . While sharing this fundamental feature, NPC1 represents its unique adaptation where it chaperones the highly hydrophobic substrate through a ~50 Å central tunnel, traversing directly from the hydrophilic lumen to the hydrophobic membrane.

It is highly plausible that many uncharacterized pathogenic variants do not merely disrupt the static protein fold, but rather perturb the substrate-induced alternating motion, delicately maintained for the lumen-to-membrane transportation. Through this lens, shifting the conceptual framework of NPC1 from a passive conduit to a dynamically coupled transport machinery not only resolves biophysical enigmas of cellular sterol trafficking but also lays a rational, mechanism-guided foundation for future therapeutics against NPC disease.

Acknowledgments

The authors acknowledge the use of Princeton's Imaging and Analysis Center (IAC), which is partially supported by the Princeton Center for Complex Materials (PCCM), a National Science Foundation (NSF) Materials Research Science and Engineering Center (MRSEC; DMR-2011750). This work was supported in part by the Ara Parseghian Medical Research Foundation (to N.Y. and X.W.). N.Y. is supported by the Shirley M. Tilghman endowed professorship from Princeton University. Molecular simulations have been supported by National Institutes of Health (grants P41-GM104601 and R24-GM145965 to ET), and using supercomputing resources provided by ACCESS (grant MCA06N060 to ET).

Author Contributions: N.Y. and X.W. conceived the project. X.W. designed the experiments, carried out the expression and purification of all proteins, cryoEM sample preparations, cryoEM data processing and structural analysis if not specified otherwise. E.T., S.D., and A.R. designed and carried out molecular dynamics simulations, as well as plotting key data figures and videos

366 for MD results. L.H.J. conceived of the bis-sterol chemical probe JM046. J.M. designed and
367 synthesized JM046, and M.A. optimized the route and synthesized the bis-sterol chemical probe.
368 X.F. ran the 3DVA program on cryoSPARC. A.P. subcloned the NPC1 sequence into pFastBac
369 vector. X.W., H.Q. and N.Y. prepared the manuscript.

370 **Competing Interest Statement:** Disclose any competing interests here.

371
372 **Materials and Methods**
373
374 ***Synthesis of bis-cholesterol molecule***

375 JM046 was synthesized through a stepwise route comprising the preparation of intermediates
376 followed by final coupling to afford JM046. Intermediates and the final product were purified by
377 silica-gel flash column chromatography, with reaction progress monitored by TLC. Structural
378 identity was verified by ^{1}H and ^{13}C NMR spectroscopy. Full experimental details and NMR data
379 are provided in the SI Appendix.

380 ***Protein expression and purification***

381 The cDNA of codon optimized human NPC1 (Uniprot: O15118) and human NPC2 (Uniprot:
382 P61916) were cloned into plasmids bearing a pCAG backbone. Both FLAG and His_{10} affinity tags
383 were added to the C-termini of the NPC proteins. HEK 293F suspension cells were grown in
384 Freestyle 293 medium (Thermo Fisher Scientific) at 37 ℃ with 5% CO_2 and 80% humidity. At a
385 density of 2.0×10^{6} cells/mL, 2 liters of cells were transiently transfected with 2 mg of NPC1 or
386 NPC2 plasmids and 6 mg polyethylenimine (PEI) (Polysciences). The NPC plasmids were
387 transfected in individual batches instead of co-transfected. Transfected cells were cultured for 48
388 h before they were harvested through 10-min centrifugation at 3,800 g.

389 The expression of hNPC1 in Sf9 cells was carried out using the Bac-to-Bac baculovirus
390 expression system. The cDNA of codon optimized human NPC1 with C-terminal FLAG and His_{10}
391 tags identical to the construct used in HEK 293F cells was cloned into the pFASTBAC1 vector
392 and transposed into DH10Bac competent cells to generate recombinant bacmids via blue/white
393 screening. Gibco Sf9 cells were cultured in Sf-900 II SFM medium (Gibco) at 27°C with constant
394 shaking (130 rpm). At the time of infection by baculovirus, the temperature was shifted to 25°C.
395 Cells were harvested after 72 h of incubation through centrifugation at 3,800 g.

396 For hNPC1 purification, the pellet after centrifugation was kept and resuspended with protease
397 inhibitors-supplemented lysis buffer (25 mM Tris pH 8.0, 150 mM NaCl, 1.3 mg/mL aprotinin, 0.7
398 mg/mL pepstatin, and 5 mg/mL leupeptin). The resuspended cells were then disrupted through
399 ultrasonication followed by an overnight incubation with 1% (w/v) DDM (Anatrace). The lysate
400 was subject to centrifugation at 27,000 g for 1 h to obtain proteins in the supernatant, which was
401 further purified through anti-FLAG M2 affinity resin (Sigma). The protein-bound resin was washed
402 with a buffer containing 25 mM Tris pH 8.0, 150 mM NaCl and 0.02% GDN (Anatrace). Elution
403 was conducted with the same buffer plus 200 μg/ml FLAG peptide. The eluate was concentrated
404 to 0.9 mL and separated through size-exclusion chromatography (SEC, Superose® 6 Increase,
405 10/300 GL, Cytiva) on ÄKTA pure (Cytiva) in the buffer containing 25 mM MES pH 5.5, 150 mM
406 NaCl, and 0.02% GDN. The eluted fractions were analyzed on SDS-PAGE, which informed
407 hNPC1-specific fractions. These fractions were concentrated to 19 mg/mL measured by
408 absorption at 280 nm.

409 For hNPC2 purification, the supernatant after centrifugation was retained as most hNPC2 was
410 secreted. After the addition of Tris pH 8.0, $NiCl_2$, and $CaCl_2$ for final concentrations of 50 mM, 4
411 mM, and 5 mM, the solution was applied to Ni-NTA affinity chromatography (resin from Qiagen).
412 Protein-bound Ni-NTA resin was washed with buffer containing 25 mM Tris pH 8.0, 150 mM NaCl

and 10 mM imidazole. Elution was conducted using the wash buffer plus 250 mM imidazole. The affinity column eluate was concentrated to 1 mL and applied to SEC (Superdex 200® Increase, 10/300 GL, Cytiva) with a low-pH SEC eluent containing 25 mM MES pH 5.5 and 150 mM NaCl. hNPC2 fractions were concentrated to 20 mg/mL measured by absorption at 280 nm.

Cryo-EM sample preparation and data collection

The purified hNPC2 was first mixed with JM046 in the low-pH buffer (25 mM MES pH 5.5 and 150 mM NaCl) at a theoretical molar ratio of 1:1 for 8 h at 4 ℃. Concentrated hNPC1 in the low-pH buffer supplemented with 0.02% GDN was then added to the solution to reach a final NPC1:NPC2:JM046 molar ratio of 1:5:5, with a final NPC1 concentration of 12 mg/mL. The mixture was kept at 4 ℃ for 8 h to allow complex formation.

Aliquots (3.5ml) of the mixture were dispensed onto glow-discharged gold Quantifoil grids (R1.2/1.3, 300 mesh). After 30 s of waiting and 5 s of blotting, the grids were plunge-frozen in liquid ethane on Vitrobot (Mark IV, ThermoFisher Scientific).

A total of 979 micrograph stacks were collected with automation programs on SerialEM (76) at 300 kV on Titan Krios equipped with K2 Summit direct electron detector (Gatan), Quantum energy filter (Gatan) and Cs corrector (Thermo Fisher). A nominal magnification of 105k × with defocus values from -2.0 μm to -1.2 μm was used. Each stack was composed of 32 frames and exposed for 5.6 s under super-resolution mode. The total dose was about 50 $e^-/Å^2$ for each stack.

Cryo-EM data processing

The collected micrograph stacks were motion-corrected, dose-weighted, defocus-estimated and binned two-fold to 1.114 Å/pixel using Warp (77) . After screening based on defocus and motion ranges, 890 micrographs were selected for downstream processing. RELION 3.0.6 was used for subsequent processing and final EM map generation (78) . Briefly, 2D classification using fast subsets followed by “deep” 2D classification (79) sorted 945,426 particles out of 3,207,444 auto-picked particles. The same batch of particles was used for 3D Variability Analysis detailed in the next paragraph. A multi-reference 3D global classification was guided by a good empirical class from a native NPC complex dataset (42) filtered to 10 Å and 3 blurry “bad” classes. Further local classification on plausible global classes narrowed good particles down to 381,411, which were 3D auto-refined and then classified without alignment, resulting in 66,353 final particles. These particles were Bayesian polished, auto-refined again with an adapted mask, and postprocessed to generate a 3D reconstruction at 3.22 Å, resolution estimated with the gold-standard Fourier shell correlation 0.143 criterion (80) with high-resolution noise substitution.

The 2D-classified particles from the same pool were taken to a single-reference 3D global classification, from which 351,867 particles were selected for non-masked 3D auto-refinement and subsequently imported to cryoSPARC (81) . The particles were re-aligned in cryoSPARC using non-uniform refinement (82), which outputted a 3.1 Å map. Data associated with this map was used as the input for 3D Variability Analysis (3DVA) (83), which resolved the motion trajectories given 3 variability components. One major conformational shift was selected and illustrated in this manuscript.

Model building and refinement

Previously reported EM structure of NPC1-8.0 at 3.0 Å (PDB: 6W5S) and crystal structure of NPC2 (PDB: 5KWY) was used as the initial models for the bis-sterol bound complex map. After docking with Chimera (84), the models were adjusted manually in Coot (85) to generate the final models. Structure refinements were carried out by PHENIX (86) in real space with secondary structure and geometry restraints.

CAVER 3.0 tunnel analysis

Water-accessible tunnels in NPC1 were computed with CAVER 3.0 (59) using a fixed starting point at the opening of the internal tunnel and a 0.9 Å probe radius. The search region was defined explicitly (shell radius 3 Å; shell depth 4 Å; automatic shell sizing disabled), and up to 10,000 candidate tunnels were evaluated per snapshot. Tunnels were clustered across snapshots by average-link hierarchical clustering with a 3.5 clustering threshold; the first 2 Å from the starting point was excluded from clustering to reduce start-site bias (minimum middle-zone length 5 Å). Tunnel-lining and bottleneck residues were assigned using a 3.0 Å contact cutoff.

Molecular dynamics simulation

All-atom molecular dynamics simulation setup

Starting from the structure of the bis-sterol NPC1-NPC2 complex, we prepared two systems: 1) NPC1-NPC2 complex with cholesterol only present in the NTD, called (NTD+CHO) condition, and, 2) NPC1-NPC2 complex with cholesterol only present in NPC2, called (NPC2+CHO) condition. Both systems were prepared for simulation using the following procedure. PSFGEN plugin in VMD (87) was used to add hydrogens and unresolved side chain atoms. Neutral N- and C-terminal caps were applied to both NPC1 and NPC2. PROPKA (88) was used for the determination of protonation states of the titratable residues.

For each system, an initial lipid bilayer was constructed after orienting the protein based on the OPM (Orientations of Proteins in Membranes) database (89). The complex was then solvated, neutralized, and 150 mM NaCl was added to the system using VMD. To have three independent replicates, the Membrane Mixer plugin in VMD (90) was used to generate two extra replicates for both NTD+CHO and NPC2+CHO systems, by randomizing the initial lipid placement. This produced three independent replicates per system.

All-atom simulation conditions

NAMD (52, 53) was used to perform the all-atom simulations using the following procedure: 1) 10,000 steps of minimization, followed by 5 ns of relaxation, where heavy atoms of protein and bound cholesterol in either NPC2 or NTD were harmonically restrained, k= 10 kcal/mol/Å^2, to their initial position; 2) 10 ns of equilibrium simulation with protein backbone restraints, k=10 kcal/mol/ Å^2; 3) 5 ns of equilibration where all restraints were decreased stepwise from 10 to 0 kcal/mol/ Å^2; 4) 500 ns of unrestrained production simulations.

All-atom simulations were performed using CHARMM36m (91) force field for protein and CHARMM36 [8] for lipids. Water was modeled using the TIP3P model (92). A 12-Å cutoff with switching starting at 10 Å was used for short-range, nonbonded interactions. Particle mesh Ewald (PME) algorithm (93) was used to model the long-range electrostatics interactions. SHAKE algorithm (94) was used to constrain bonds to hydrogen atoms. Langevin thermostat was employed to maintain the temperature at 310 K, while pressure was set to 1 atm using the Nose-Hoover piston barostat with a period of 100 fs and a decay of 50 fs (95, 96). Integration was performed with a timestep set to 2 fs.

All-atom simulation analysis

To quantify the movement of NPC2 and NTD domains under (NPC2+CHO) and (NTD+CHO) conditions, the angle between the membrane normal and the vector that connects the center of mass (CoM) of NPC2-V57 and CoM of NPC2-L78 is defined as $\boldsymbol{\alpha}$, and that between the membrane normal and the vector connecting the CoMs of NPC1-Q79 and NPC1-L176 is defined as β. To further quantify the relative motion between NTD and domain I, the distance between CoM of residues within 6 Å of the tail of the bound cholesterol (Fig S3A) in the NTD, residues L89,

P176, Y192, M193, N198, Q200, and CoM of the triple Asn, N944, N975, and N948 were measured.

Next, to quantify the kink angle in the Neck helix 2 and the TM2 under the NPC2-CHO and NTD-CHO conditions, θ is defined as the angle between the first principal axes of the backbone atoms of R607--D618 (representing Neck helix 2) and those of F622-L637 (representing TM2).

Coarse-Grained (CG) molecular dynamics simulation setup

CG MD simulations utilized the MARTINI force field (97, 98), applying a 4:1 heavy-atom mapping scheme. The simulation box (400 × 400 Å in the xy-plane) contained four identical protein replicas spaced 200 Å apart to ensure independent local lipid sampling environments. The lipid bilayer was composed of POPC/DOPG/DPSM/Cholesterol at a molar ratio of 70:10:10:10.

CG molecular dynamics simulation conditions

Simulations were executed in GROMACS (99). An integration time step of 20 fs was used. The protocol involved an initial equilibration with position restraints on both the protein and lipids. For the production runs, backbone position restraints were maintained to prevent overall rotation and translation of the proteins. The multi-replica system was simulated for a single continuous 20 μs trajectory (resulting in 80 μs of effective protein-lipid interaction sampling).

CG molecular dynamics simulation analysis

Trajectory analysis focused on cholesterol clustering at the SSD and SSDL domains. A distance cutoff of 7 Å between the CG beads of cholesterol and the protein surface was used to define contact and quantify the number of bound sterol molecules over time.

References

1. J. P. Davies, B. Levy, Y. A. Ioannou, Evidence for a Niemann–Pick C (NPC) Gene Family: Identification and Characterization of NPC1L1. *Genomics* **65**, 137–145 (2000).

2. Y. A. Ioannou, Guilty until proven innocent: the case of NPC1 and cholesterol. *Trends Biochem Sci* **30**, 498–505 (2005).

3. D. E. Sleat, *et al.*, Genetic evidence for nonredundant functional cooperativity between NPC1 and NPC2 in lipid transport. *P Natl Acad Sci Usa* **101**, 5886–5891 (2004).

4. K. Subramanian, W. E. Balch, NPC1/NPC2 function as a tag team duo to mobilize cholesterol. *Proc National Acad Sci* **105**, 15223–15224 (2008).

5. P. G. Pentchev, *et al.*, The Niemann-Pick C lesion and its relationship to the intracellular distribution and utilization of LDL cholesterol. *Biochimica Et Biophysica Acta Bba - Mol Basis Dis* **1225**, 235–243 (1994).

6. E. D. Carstea, *et al.*, Niemann-Pick C1 Disease Gene: Homology to Mediators of Cholesterol Homeostasis. *Science* **277**, 228–231 (1997).

7. M. T. Vanier, Niemann-Pick disease type C. *Orphanet J Rare Dis* **5**, 1–18 (2010).

8. T. Geberhiwot, *et al.*, Consensus clinical management guidelines for Niemann-Pick disease type C. *Orphanet J Rare Dis* **13**, 50 (2018).

9. M. C. Patterson, *et al.*, Long-term survival outcomes of patients with Niemann-Pick disease type C receiving miglustat treatment: A large retrospective observational study. *J Inherit Metab Dis* **43**, 1060–1069 (2020).

10. M. Vanier, G. Millat, Niemann–Pick disease type C. *Clin Genet* **64**, 269–281 (2003).

11. M. C. Patterson, *et al.*, Recommendations for the diagnosis and management of Niemann–Pick disease type C: An update. *Mol Genet Metab* **106**, 330–344 (2012).

12. B. J. H. M. Poorthuis, *et al.*, The frequency of lysosomal storage diseases in The Netherlands. *Hum Genet* **105**, 151–156 (1999).

13. M. Labrecque, L. Touma, C. Bhérer, A. Duquette, M. Tétreault, Estimated prevalence of Niemann–Pick type C disease in Quebec. *Sci Rep-uk* **11**, 22621 (2021).

14. R. Pinto, *et al.*, Prevalence of lysosomal storage diseases in Portugal. *Eur J Hum Genet* **12**, 87–92 (2004).

15. A. C. CROCKER, S. FARBER, NIEMANN-PICK DISEASE. *Medicine* **37**, 1 (1958).

16. C. A. Wassif, *et al.*, High incidence of unrecognized visceral/neurological late-onset Niemann-Pick disease, type C1, predicted by analysis of massively parallel sequencing data sets. *Genet Med* **18**, 41 (2016).

17. F. M. Platt, G. R. Neises, R. A. Dwek, T. D. Butters, N-butyldeoxynojirimycin is a novel inhibitor of glycolipid biosynthesis. *J Biological Chem* **269**, 8362–5 (1994).

18. M. C. Patterson, D. Vecchio, H. Prady, L. Abel, J. E. Wraith, Miglustat for treatment of Niemann-Pick C disease: a randomised controlled study. *Lancet Neurology* **6**, 765–772 (2007).

19. M. Pineda, M. Walterfang, M. C. Patterson, Miglustat in Niemann-Pick disease type C patients: a review. *Orphanet J Rare Dis* **13**, 140 (2018).

20. M. L. Heras, *et al.*, Understanding the phenotypic variability in Niemann-Pick disease type C (NPC): a need for precision medicine. *npj Genom. Med.* **8**, 21 (2023).

21. F. D. Porter, *et al.*, Cholesterol Oxidation Products Are Sensitive and Specific Blood-Based Biomarkers for Niemann-Pick C1 Disease. *Sci Transl Med* **2**, 56ra81 (2010).

22. T. J. Maarup, *et al.*, Intrathecal 2-hydroxypropyl-beta-cyclodextrin in a single patient with Niemann–Pick C1. *Mol Genet Metab* **116**, 75–79 (2015).

23. J. E. Megías-Vericat, *et al.*, Early experience with compassionate use of 2 hydroxypropyl-beta-cyclodextrin for Niemann–Pick type C disease: review of initial published cases. *Neurol Sci* **38**, 727–743 (2017).

24. L. Abi-Mosleh, R. E. Infante, A. Radhakrishnan, J. L. Goldstein, M. S. Brown, Cyclodextrin overcomes deficient lysosome-to-endoplasmic reticulum transport of cholesterol in Niemann-Pick type C cells. *Proc National Acad Sci* **106**, 19316–19321 (2009).

25. T.-Y. Chang, *et al.*, Niemann-Pick Type C Disease and Intracellular Cholesterol Trafficking. *Journal of Biological Chemistry* **280**, 20917–20920 (2005).

26. J. L. Goldstein, S. E. Dana, J. R. Faust, A. L. Beaudet, M. S. Brown, Role of lysosomal acid lipase in the metabolism of plasma low density lipoprotein. Observations in cultured fibroblasts from a patient with cholesteryl ester storage disease. *J Biological Chem* **250**, 8487–95 (1975).

27. J. P. Davies, Y. A. Ioannou, Topological analysis of NPC1 reveals that the orientation of the putative sterol sensing domain is identical to that of HMG CoA and SCAP. *J Biol Chem* **275**, 24367–24374 (2000).

28. C. Scott, Y. A. Ioannou, The NPC1 protein: structure implies function. *Biochimica Et Biophysica Acta Bba - Mol Cell Biology Lipids* **1685**, 8–13 (2004).

29. W. D. Park, *et al.*, Identification of 58 novel mutations in Niemann-Pick disease type C: Correlation with biochemical phenotype and importance of PTC1-like domains in NPC1. *Hum Mutat* **22**, 313–325 (2003).

30. E. Ikonen, Cellular cholesterol trafficking and compartmentalization. *Nat Rev Mol Cell Bio* **9**, 125–138 (2008).

31. K. Simons, E. Ikonen, How Cells Handle Cholesterol. *Science* **290**, 1721–1726 (2000).

32. S. Naureckiene, *et al.*, Identification of HE1 as the Second Gene of Niemann-Pick C Disease. *Science* **290**, 2298–2301 (2000).

33. M. T. Vanier, G. Millat, Structure and function of the NPC2 protein. *Biochimica Et Biophysica Acta Bba - Mol Cell Biology Lipids* **1685**, 14–21 (2004).

34. J. Storch, Z. Xu, Niemann–Pick C2 (NPC2) and intracellular cholesterol trafficking. *Biochimica Et Biophysica Acta Bba - Mol Cell Biology Lipids* **1791**, 671–678 (2009).

35. M. S. Deffieu, S. R. Pfeffer, Niemann–Pick type C 1 function requires lumenal domain residues that mediate cholesterol-dependent NPC2 binding. *Proc National Acad Sci* **108**, 18932–18936 (2011).

36. S. Xu, B. Benoff, H.-L. Liou, P. Lobel, A. M. Stock, Structural Basis of Sterol Binding by NPC2, a Lysosomal Protein Deficient in Niemann-Pick Type C2 Disease. *J Biol Chem* **282**, 23525–23531 (2007).

37. R. E. Infante, *et al.*, Purified NPC1 Protein I. BINDING OF CHOLESTEROL AND OXYSTEROLS TO A 1278-AMINO ACID MEMBRANE PROTEIN. *J Biol Chem* **283**, 1052–1063 (2008).

38. R. E. Infante, *et al.*, Purified NPC1 Protein II. LOCALIZATION OF STEROL BINDING TO A 240-AMINO ACID SOLUBLE LUMINAL LOOP. *J Biol Chem* **283**, 1064–1075 (2008).

39. H. J. Kwon, *et al.*, Structure of N-Terminal Domain of NPC1 Reveals Distinct Subdomains for Binding and Transfer of Cholesterol. *Cell* **137**, 1213–1224 (2009).

40. R. E. Infante, *et al.*, NPC2 facilitates bidirectional transfer of cholesterol between NPC1 and lipid bilayers, a step in cholesterol egress from lysosomes. *Proc National Acad Sci* **105**, 15287–15292 (2008).

608 41. X. Li, P. Saha, J. Li, G. Blobel, S. R. Pfeffer, Clues to the mechanism of cholesterol transfer from the
609 structure of NPC1 middle lumenal domain bound to NPC2. *Proc National Acad Sci* **113**, 10079–10084
610 (2016).

611 42. H. Qian, *et al.*, Structural Basis of Low-pH-Dependent Lysosomal Cholesterol Egress by NPC1 and
612 NPC2. *Cell* **182**, 98-111.e18 (2020).

613 43. M. L. Wang, *et al.*, Identification of Surface Residues on Niemann-Pick C2 Essential for Hydrophobic
614 Handoff of Cholesterol to NPC1 in Lysosomes. *Cell Metab* **12**, 166–173 (2010).

615 44. N. Friedland, H.-L. Liou, P. Lobel, A. M. Stock, Structure of a cholesterol-binding protein deficient in
616 Niemann–Pick type C2 disease. *Proc National Acad Sci* **100**, 2512–2517 (2002).

617 45. X. Gong, *et al.*, Structural Insights into the Niemann-Pick C1 (NPC1)-Mediated Cholesterol Transfer
618 and Ebola Infection. *Cell* **165**, 1467–1478 (2016).

619 46. X. Li, *et al.*, 3.3 Å structure of Niemann–Pick C1 protein reveals insights into the function of the C-
620 terminal luminal domain in cholesterol transport. *Proc National Acad Sci* **114**, 9116–9121 (2017).

621 47. X. Li, *et al.*, Structure of human Niemann–Pick C1 protein. *Proc National Acad Sci* **113**, 8212–8217
622 (2016).

623 48. V. Dubey, B. Bozorg, D. Wüstner, H. Khandelia, Cholesterol binding to the sterol-sensing region of
624 Niemann Pick C1 protein confines dynamics of its N-terminal domain. *Plos Comput Biol* **16**, e1007554
625 (2020).

626 49. C.-S. Huang, *et al.*, Cryo-EM structures of NPC1L1 reveal mechanisms of cholesterol transport and
627 ezetimibe inhibition. *Sci Adv* **6**, eabb1989 (2020).

628 50. K. M. Frain, *et al.*, Conformational changes in the Niemann–Pick type C1 protein NCR1 drive sterol
629 translocation. *Proc. Natl. Acad. Sci.* **121**, e2315575121 (2024).

630 51. T. Long, Y. Liu, Y. Qin, R. A. DeBose-Boyd, X. Li, Structures of dimeric human NPC1L1 provide
631 insight into mechanisms for cholesterol absorption. *Sci Adv* **7**, eabh3997 (2021).

632 52. J. C. Phillips, *et al.*, Scalable molecular dynamics on CPU and GPU architectures with NAMD. *J. Chem.*
633 *Phys.* **153**, 044130 (2020).

634 53. J. C. Phillips, *et al.*, Scalable molecular dynamics with NAMD. *J. Comput. Chem.* **26**, 1781–802 (2005).

635 54. M. Silberkang, C. M. Havel, D. S. Friend, B. J. McCarthy, J. A. Watson, Isoprene synthesis in isolated
636 embryonic Drosophila cells. I. Sterol-deficient eukaryotic cells. *J. Biol. Chem.* **258**, 8503–8511 (1983).

637 55. G. Vinci, X. Xia, R. A. Veitia, Preservation of Genes Involved in Sterol Metabolism in Cholesterol
638 Auxotrophs: Facts and Hypotheses. *PLoS ONE* **3**, e2883 (2008).

639 56. K. Marheineke, S. Grünewald, W. Christie, H. Reiländer, Lipid composition of Spodoptera frugiperda
640 (Sf9) and Trichoplusia ni (Tn) insect cells used for baculovirus infection. *FEBS Lett.* **441**, 49–52 (1998).

641 57. V. Cherezov, *et al.*, High-Resolution Crystal Structure of an Engineered Human β_2-Adrenergic G
642 Protein–Coupled Receptor. *Science* **318**, 1258–1265 (2007).

643 58. X. Wu, R. Yan, P. Cao, H. Qian, N. Yan, Structural advances in sterol-sensing domain-containing
644 proteins. *Trends Biochem Sci* **47**, 289–300 (2022).

645 59. E. Chovancova, *et al.*, CAVER 3.0: A Tool for the Analysis of Transport Pathways in Dynamic Protein
646 Structures. *Plos Comput Biol* **8**, e1002708 (2012).

647 60. S. W. Altmann, *et al.*, Niemann-Pick C1 Like 1 Protein Is Critical for Intestinal Cholesterol Absorption.
648 *Science* **303**, 1201–1204 (2004).

649 61. D. S. Schade, L. Shey, R. P. Eaton, Cholesterol Review: A Metabolically Important Molecule. *Endocr*
650 *Pract* **26**, 1514–1523 (2020).

651 62. L. Ge, *et al.*, Flotillins play an essential role in Niemann-Pick C1-like 1-mediated cholesterol uptake.
652 *Proc National Acad Sci* **108**, 551–556 (2011).

653 63. M. Hu, *et al.*, Structural insights into the mechanism of human NPC1L1-mediated cholesterol uptake.
654 *Sci Adv* **7**, eabg3188 (2021).

655 64. K. Kazmier, D. P. Claxton, H. S. Mchaourab, Alternating access mechanisms of LeuT-fold transporters:
656 trailblazing towards the promised energy landscapes. *Curr Opin Struc Biol* **45**, 100–108 (2017).

657 65. D. Drew, R. A. North, K. Nagarathinam, M. Tanabe, Structures and General Transport Mechanisms by
658 the Major Facilitator Superfamily (MFS). *Chem. Rev.* **121**, 5289–5335 (2021).

659 66. Y. Shi, Common Folds and Transport Mechanisms of Secondary Active Transporters. *Annu. Rev.*
660 *Biophys.* **42**, 51–72 (2013).

661 67. W. F. Neiss, A coat of glycoconjugates on the inner surface of the lysosomal membrane in the rat
662 kidney. *Histochemistry* **80**, 603–608 (1984).

663 68. M. Kosicek, *et al.*, N-glycome of the Lysosomal Glycocalyx is Altered in Niemann-Pick Type C
664 Disease (NPC) Model Cells*. *Mol. Cell. Proteom.* **17**, 631–642 (2018).

665 69. R. Liu, P. Lu, J. W. K. Chu, F. J. Sharom, Characterization of Fluorescent Sterol Binding to Purified
666 Human NPC1. *J Biol Chem* **284**, 1840–1852 (2009).

667 70. H. Nikaido, Y. Takatsuka, Mechanisms of RND multidrug efflux pumps. *Biochimica Et Biophysica*
668 *Acta Bba - Proteins Proteom* **1794**, 769–781 (2009).

669 71. L. Yu, W. Lu, Y. Wei, AcrB Trimer Stability and Efflux Activity, Insight from Mutagenesis Studies.
670 *Plos One* **6**, e28390 (2011).

671 72. M. C. Sulavik, *et al.*, Antibiotic Susceptibility Profiles of Escherichia coli Strains Lacking Multidrug
672 Efflux Pump Genes. *Antimicrob Agents Ch* **45**, 1126–1136 (2001).

673 73. W. Lu, *et al.*, Assembling of AcrB Trimer in Cell Membrane. *J Mol Biol* **423**, 123–134 (2012).

674 74. H. I. Zgurskaya, H. Nikaido, Bypassing the periplasm: Reconstitution of the AcrAB multidrug efflux
675 pump of Escherichia coli. *Proceedings of the National Academy of Sciences* **96** (1999).

75. J. Kobylka, M. S. Kuth, R. T. Müller, E. R. Geertsma, K. M. Pos, AcrB: a mean, keen, drug efflux machine. *Ann. N. York Acad. Sci.* **1459**, 38–68 (2020).

76. D. N. Mastronarde, SerialEM: A Program for Automated Tilt Series Acquisition on Tecnai Microscopes Using Prediction of Specimen Position. *Microsc. Microanal.* **9**, 1182–1183 (2003).

77. D. Tegunov, P. Cramer, Real-time cryo-electron microscopy data preprocessing with Warp. *Nat. Methods* **16**, 1146–1152 (2019).

78. S. H. W. Scheres, RELION: Implementation of a Bayesian approach to cryo-EM structure determination. *J Struct Biol* **180**, 519–530 (2012).

79. X. Yao, X. Fan, N. Yan, Cryo-EM analysis of a membrane protein embedded in the liposome. *Proc. Natl. Acad. Sci.* **117**, 18497–18503 (2020).

80. P. B. Rosenthal, R. Henderson, Optimal Determination of Particle Orientation, Absolute Hand, and Contrast Loss in Single-particle Electron Cryomicroscopy. *J Mol Biol* **333**, 721–745 (2003).

81. A. Punjani, J. L. Rubinstein, D. J. Fleet, M. A. Brubaker, cryoSPARC: algorithms for rapid unsupervised cryo-EM structure determination. *Nat Methods* **14**, 290–296 (2017).

82. A. Punjani, H. Zhang, D. J. Fleet, Non-uniform refinement: adaptive regularization improves single-particle cryo-EM reconstruction. *Nat. Methods* **17**, 1214–1221 (2020).

83. A. Punjani, D. J. Fleet, 3D variability analysis: Resolving continuous flexibility and discrete heterogeneity from single particle cryo-EM. *J Struct Biol* **213**, 107702 (2021).

84. E. F. Pettersen, *et al.*, UCSF Chimera—A visualization system for exploratory research and analysis. *J. Comput. Chem.* **25**, 1605–1612 (2004).

85. P. Emsley, B. Lohkamp, W. G. Scott, K. Cowtan, Features and development of Coot. *Acta Crystallogr Sect D* **66**, 486–501 (2010).

86. P. D. Adams, *et al.*, PHENIX: a comprehensive Python-based system for macromolecular structure solution. *Acta Crystallogr Sect D Biological Crystallogr* **66**, 213–221 (2010).

87. W. Humphrey, A. Dalke, K. Schulten, VMD: Visual molecular dynamics. *J. Mol. Graph.* **14**, 33–38 (1996).

88. M. H. M. Olsson, C. R. Søndergaard, M. Rostkowski, J. H. Jensen, PROPKA3: Consistent Treatment of Internal and Surface Residues in Empirical pKa Predictions. *J. Chem. theory Comput.* **7**, 525–37 (2011).

89. M. A. Lomize, A. L. Lomize, I. D. Pogozheva, H. I. Mosberg, OPM: Orientations of Proteins in Membranes database. *Bioinformatics* **22**, 623–625 (2006).

90. G. Licari, S. Dehghani-Ghahnaviyeh, E. Tajkhorshid, Membrane Mixer: A Toolkit for Efficient Shuffling of Lipids in Heterogeneous Biological Membranes. *J. Chem. Inf. Model.* **62**, 986–996 (2022).

91. J. B. Klauda, *et al.*, Update of the CHARMM All-Atom Additive Force Field for Lipids: Validation on Six Lipid Types. *J. Phys. Chem. B* **114**, 7830–7843 (2010).

92. W. L. Jorgensen, J. Chandrasekhar, J. D. Madura, R. W. Impey, M. L. Klein, Comparison of simple potential functions for simulating liquid water. *J. Chem. Phys.* **79**, 926–935 (1983).

93. T. Darden, D. York, L. Pedersen, Particle mesh Ewald: An N ·log(N) method for Ewald sums in large systems. *J. Chem. Phys.* **98**, 10089–10092 (1993).

94. J.-P. Ryckaert, G. Ciccotti, H. J. C. Berendsen, Numerical integration of the cartesian equations of motion of a system with constraints: molecular dynamics of n-alkanes. *J. Comput. Phys.* **23**, 327–341 (1977).

95. G. J. Martyna, D. J. Tobias, M. L. Klein, Constant pressure molecular dynamics algorithms. *J. Chem. Phys.* **101**, 4177–4189 (1994).

96. S. E. Feller, Y. Zhang, R. W. Pastor, B. R. Brooks, Constant pressure molecular dynamics simulation: The Langevin piston method. *J. Chem. Phys.* **103**, 4613–4621 (1995).

97. S. J. Marrink, H. J. Risselada, S. Yefimov, D. P. Tieleman, A. H. de Vries, The MARTINI Force Field: Coarse Grained Model for Biomolecular Simulations. *J. Phys. Chem. B* **111**, 7812–7824 (2007).

98. D. H. de Jong, *et al.*, Improved Parameters for the Martini Coarse-Grained Protein Force Field. *J. Chem. Theory Comput.* **9**, 687–697 (2013).

99. M. J. Abraham, *et al.*, GROMACS: High performance molecular simulations through multi-level parallelism from laptops to supercomputers. *SoftwareX* **1**, 19–25 (2015).

Figures and Tables

Figure 1. Structure of the bis-sterol bound NPC1-NPC2 complex. A. Schematic representation of the cholesterol transfer cycle from NPC2 to NTD and the proposed role of the bis-sterol molecules in stabilizing the transient state of cholesterol transfer. **B, C.** Cryo-EM map (**B**) and corresponding molecular model (**C**) of the bis-sterol bound NPC1-NPC2 complex. **D.** Structural comparison of native NPC1-NPC2 complex (gray) and the bis-sterol bound NPC1-NPC2 complexes (color). The structures are aligned relative to the domain C in each complex. *Inset*: A zoomed-in view of NPC2 and NTD highlighting the movement of NPC2 towards to NTD in the bis-sterol structure. **E.** Structural overlays of the native complex and the bis-sterol bound complex for the NPC2-domain C (left) and NTD-domain I (right) regions.

Figure 2. Molecular dynamics simulations based on bis-sterol bound complex structure. A. Illustrated definition of α and β angles in these simulations. Rose balls: CoM coordinates that form the vectors by which the angles are defined. **B.** Distribution of α and β throughout the simulations with two starting conditions, under which cholesterol is either only present and fixed in the NPC2 pocket (red, NPC2+CHO) or in the NTD pocket (blue, NTD+CHO). Dashed lines: starting position based on the cryo-EM structure of bis-sterol bound complex. **C.** β angle values of 3 replicates over the course of the 500-ns simulations. Dashed lines: starting position based on bis-sterol bound complex structure. **D.** Illustrated definition of the distance between NTD and domain I. Rose balls: CoM coordinates by which the distance is defined. **E.** Histograms comparing the distance of NTD-domain I in the NPC2+CHO (red) and NTD+CHO (blue) simulations. Dashed lines: starting distances based on the bis-sterol bound complex structure.

Figure 3. Structural comparisons between the contracted and expanded conformation of NPC1 at different structures. **A.** Overlaid maps of the native and bis-sterol bound NPC1-NPC2 complexes showing distinctions in cholesterol occupancy in the tunnel (top right) and helices displacement in the neck region (bottom right). The structural movement was indicated by black arrows. Both maps are displayed at σ=7. **B.** Molecular structures of native and bis-sterol bound complexes overlaid in the NPC1 region with NPC2 hidden. *Insets*: close examination of the cholesterol-bearing lower tunnel (top) and model comparison of the two complexes over the TM helices (middle and bottom). The curved arrow indicates the potential exit path for cholesterol release from the tunnel. **C**. The starting and ending fames of 3DVA volume series overlaid, showing a similar pattern in helical displacement at Neck Helix 2-TM2. **D.** Overlaid maps of lone NPC1 expressed in Sf9 cells (colors) and HEK293F cells (grey) show distinctions in cholesterol occupancy in lower tunnel and helices displacement in the neck region (inset); both maps are at σ=7.

Figure 4. Speculated cholesterol exit path and the "alternating access" model of substrate-induced conformation shifts. A. Structures of equilibrated MD models under the NPC2+CHO and NTD+CHO simulated conditions. These two MD models are referred as NPC1-NPC2 (MD, NPC2+CHO) and NPC1-NPC2 (MD, NTD+CHO), respectively. *Inset:* two structures overlaid at the neck site, with NPC1-NPC2 (MD, NTD+CHO) colored in grey for clear comparison. **B.** Illustrated definition of θ angle (left) and its distribution over simulations under NPC2+CHO (red) and NTD+CHO conditions (blue) (right). **C.** Kink angle θ values over the course of the 500-ns simulations, all 3 replicas displayed. **D.** Results of Caver 3.0 (59) tunnel searches, in dark brown mesh, inside 3 NPC1-NPC2 complex models including the native, bis-sterol bound, and equilibrated MD structure when cholesterol is loaded in NPC2 only (NPC2+CHO). Structures showed from left to right from the most contracted to the most expanded. This order is aligned with a trend of narrowing upper tunnel and dilating lower tunnel. Pink ball: Cα of N614 as a marker for tunnel exit to SSD; black arrows: increasing radii at the tunnel exits. **E.** Simulated

782 sterol affinitive “hot spots”, displayed in purple mesh, across NPC1 TM domains predicts
783 locations along the SSD hydrophobic groove where cholesterol might transiently interact during
784 its exit. **F.** The “alternating access model” proposes that the two conformers of NPC1 observed in
785 various conditions are induced by substrate binding in a spatial-temporal order. The dynamics of
786 NPC2 cholesterol handoff, NTD docking and neck expansion are a series of meaningful events
787 contributing to a functional NPC-mediated cholesterol delivery system.

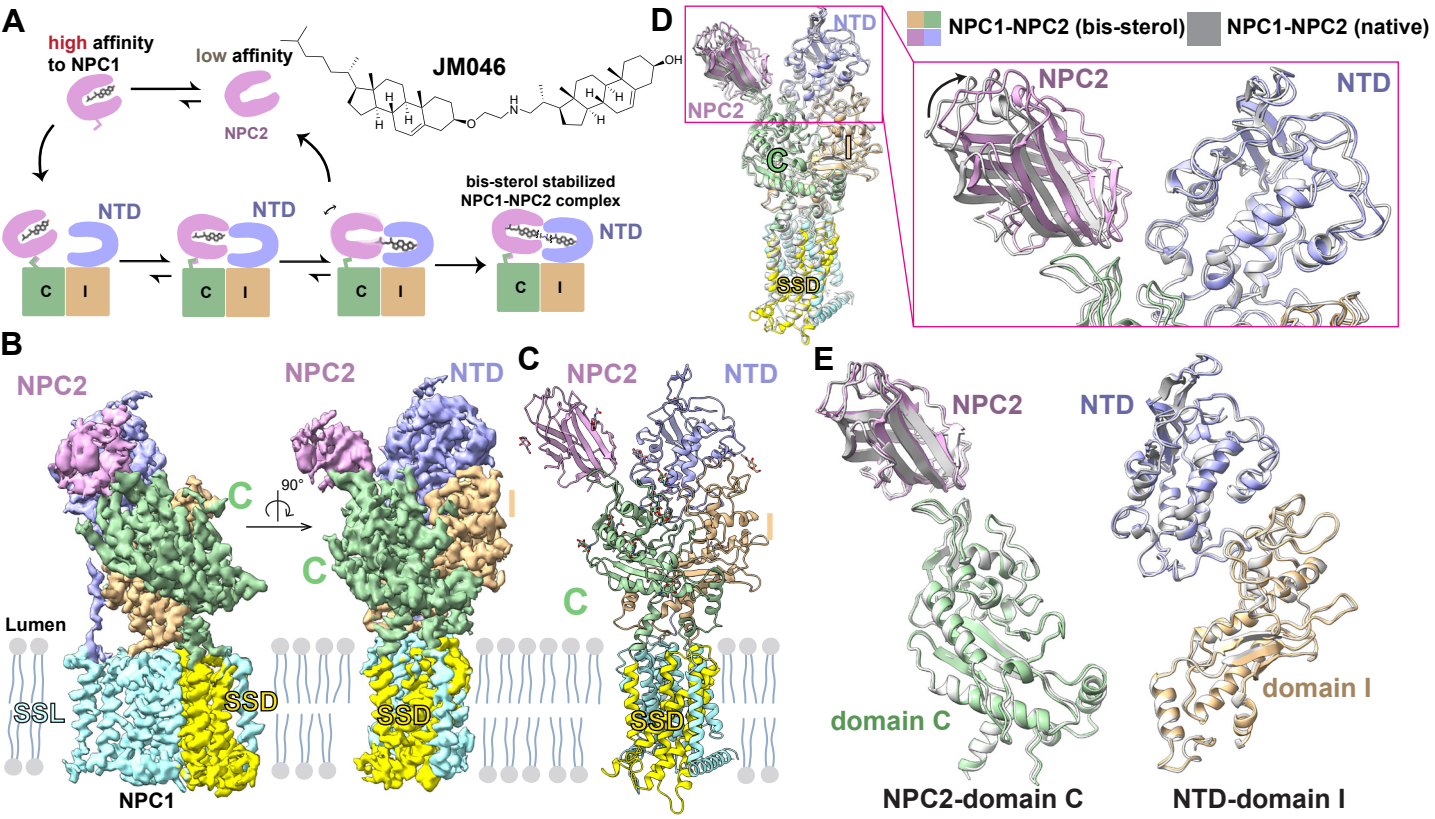
A
high affinity to NPC1
low affinity
NPC2
JM046
NTD
C
I
bis-sterol stabilized NPC1-NPC2 complex
B
NPC2
NTD
90°
Lumen
SSL
SSD
NPC1
C
D
NPC1-NPC2 (bis-sterol)
NPC1-NPC2 (native)
SSD
E
domain C
domain I
NPC2-domain C
NTD-domain I

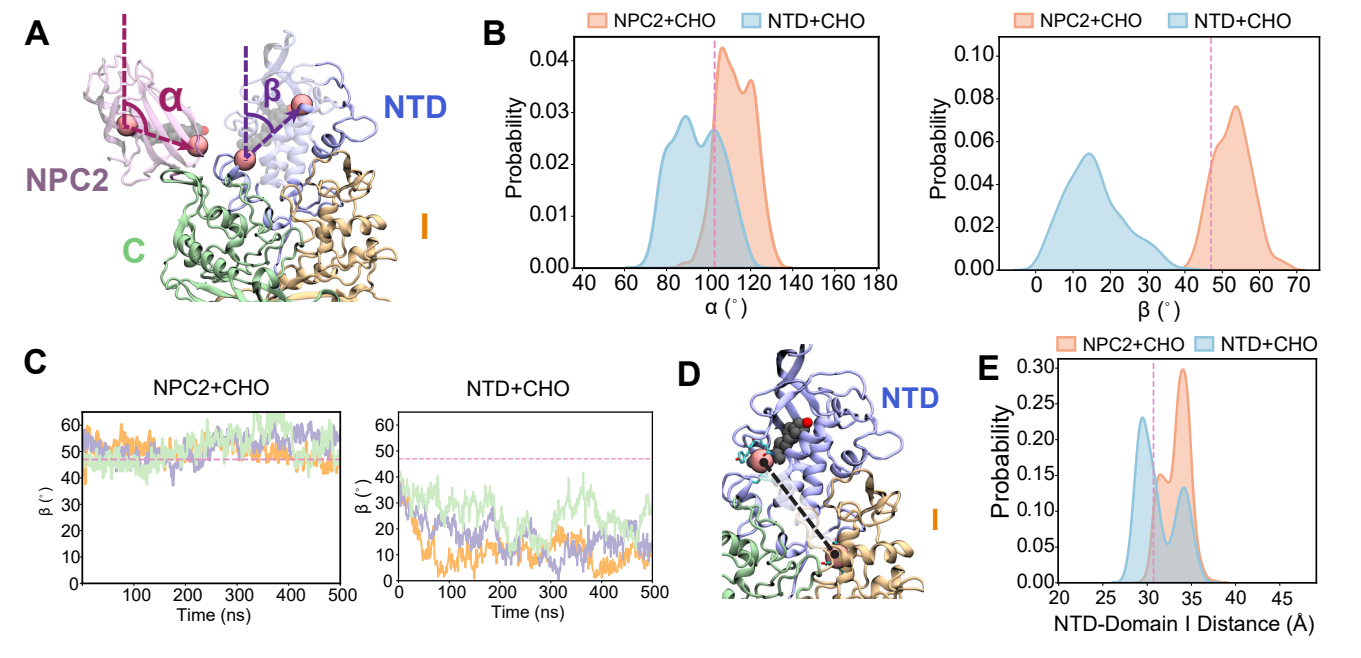
A
α
β
NTD
NPC2
C
I
B
NPC2+CHO
NTD+CHO
Probability
α (°)
β (°)
C
NPC2+CHO
NTD+CHO
β (°)
Time (ns)
D
NTD
I
E
NPC2+CHO
NTD+CHO
Probability
NTD-Domain I Distance (Å)

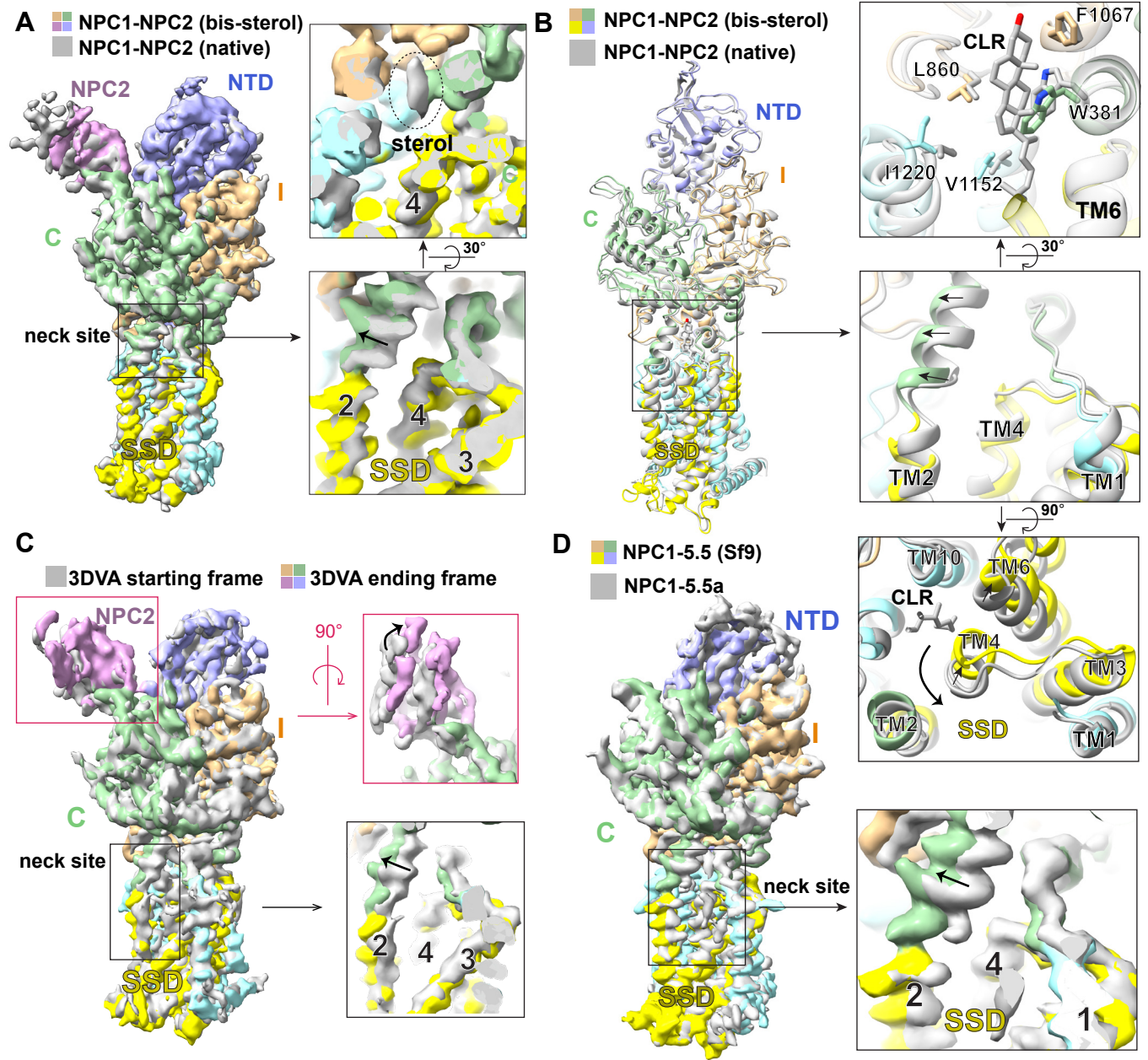
A
NPC1-NPC2 (bis-sterol)
NPC1-NPC2 (native)
NPC2
NTD
I
C
neck site
SSD
sterol
4
30°
2
4
SSD
3
B
NPC1-NPC2 (bis-sterol)
NPC1-NPC2 (native)
NTD
I
C
SSD
F1067
CLR
L860
W381
I1220
V1152
TM6
30°
TM4
TM2
TM1
90°
C
3DVA starting frame
3DVA ending frame
NPC2
I
C
neck site
SSD
90°
2
4
3
D
NPC1-5.5 (Sf9)
NPC1-5.5a
NTD
I
C
neck site
SSD
TM10
TM6
CLR
TM4
TM3
TM2
SSD
TM1
4
2
SSD
1

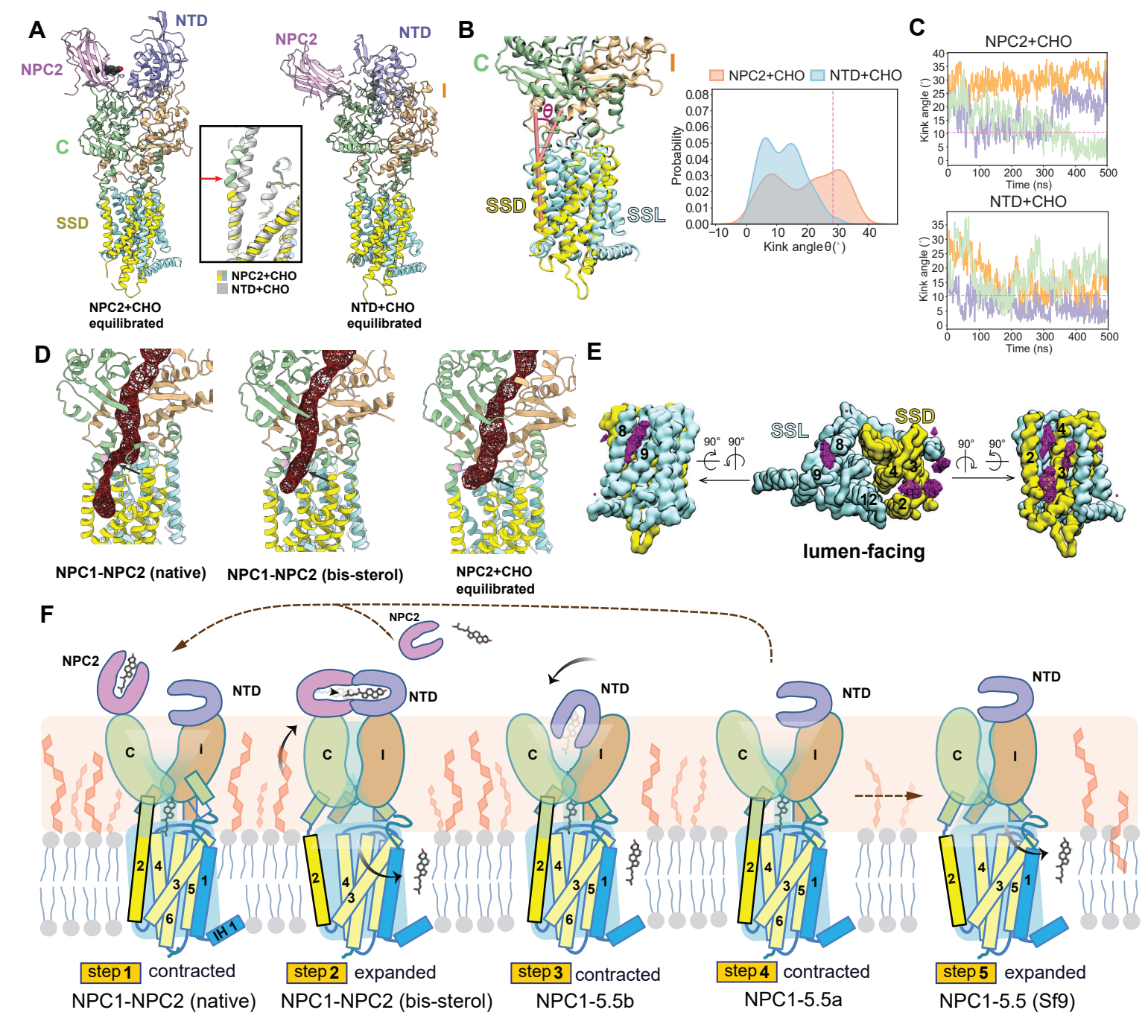
A
NTD
NPC2
C
SSD
NPC2
NTD
I
NPC2+CHO
NTD+CHO
NPC2+CHO
equilibrated
NTD+CHO
equilibrated
B
C
I
θ
SSD
SSL
NPC2+CHO
NTD+CHO
Probability
Kink angle θ(°)
C
NPC2+CHO
NTD+CHO
Kink angle (°)
Time (ns)
D
NPC1-NPC2 (native)
NPC1-NPC2 (bis-sterol)
NPC2+CHO
equilibrated
E
SSL
SSD
90°
90°
lumen-facing
F
NPC2
NTD
C
I
IH 1
step 1 contracted
NPC1-NPC2 (native)
step 2 expanded
NPC1-NPC2 (bis-sterol)
step 3 contracted
NPC1-5.5b
step 4 contracted
NPC1-5.5a
step 5 expanded
NPC1-5.5 (Sf9)